RESEARCH ARTICLE | OCTOBER 01 2024

Superimposed squeeze and rotational flows of Newtonian and power-law fluids [a)]

[a)]Dedicated to Nicolás M. Páez-Flor, Ph.D. In memoriam (1983–2023).

F. J. Rubio-Hernández ; J. F. Velázquez-Navarro ; M. Rodríguez-Lara

J. Rheol. 68, 863–872 (2024)
https://doi.org/10.1122/8.0000887

Superimposed squeeze and rotational flows of Newtonian and power-law fluids[a)]

F. J. Rubio-Hernández,[1,b)] J. F. Velázquez-Navarro,[2] and M. Rodríguez-Lara[1]

[1]*Department of Applied Physics II, University of Málaga, Málaga, Spain*
[2]*Department of Mechanics, Thermal, and Fluids Engineering, University of Málaga, Málaga, Spain*

(Received 31 May 2024; final revision received 12 September 2024; published 1 October 2024)

Abstract

This study theoretically predicted the response of superimposed squeeze and rotational flows (SSRF) of fluids with different viscous behaviors (i.e., Newtonian, shear-thinning, and shear-thickening fluids). The theoretical predictions were verified using the plate-plate geometry for the SSRF measurements with the Newtonian and power-law fluids. In all the cases, the squeeze force increased as the gap decreased, but the response was very different for each rheological behavior. The variation in the squeeze force with the gap was not affected by the superimposed rotational shear stress value, owing to the nondependency of the viscosity on the shear for Newtonian fluids. However, for the power-law fluids, the squeeze force variation with the gap value was based on the value of the superimposed shear stress value. The decrease and increase in the viscosity with the shear stress for the shear-thinning and shear-thickening fluids, respectively, resulted in opposite trends of the squeeze force with the gap value variation. For the shear-thinning fluids, the squeeze force for each gap value decreased with increasing superimposed rotational shear stress. The opposite trend was observed for the shear-thickening fluid. In the absence of wall slip, the theoretical predictions well agreed with the experimental results.
https://doi.org/10.1122/8.0000887

I. INTRODUCTION

When two coaxial parallel plates with a fluid between them approach each other, a squeeze flow is afforded. Squeeze flows assist in the rheological characterization of matter and can be very useful in material processing. Although the squeeze flows of Newtonian and shear-thinning fluids have been extensively analyzed theoretically [1–3] and experimentally [4–8], those of shear-thickening fluids have not been comprehensively analyzed [9].

Squeeze flows are unavoidably intermixed with shear flows; hence, flow conditions that are more complex than the conventional simple shear flow conditions should be included in the rheological characterization of fluids. For example, a device capable of superimposing oscillatory squeeze and oscillatory rotational flows has been proposed for characterizing the viscoelastic response of fluids [10]. This study focused on the response of superimposed squeeze and rotational flows (SSRF) of fluids with different viscous behaviors (Newtonian, shear-thinning, and shear-thickening fluids). SSRF were realized with a plate-plate geometry because this geometry is representative of different practical situations, such as those appearing in damping, antivibration, or absorbing impact devices. Using the SSRF rheological test, a first-order approximation for the three-dimensional (3D) description of the viscous flow behavior of fluids can be obtained [11]. Since a wall slip influences the recorded squeeze force [12,13], nonslip conditions should be checked. Under steady-state conditions, two independent components of the rate-of-strain tensor ($\dot{\gamma}$) develop during the SSFR rheological test: the rotation of the upper plate around the common axis induces a shear rate $\dot{\gamma}_{\theta z}$, and the squeeze flow of the upper plate toward the down plate induces a radial shear rate $\dot{\gamma}_{rz}$.

First, the theoretical SSRF problem was analytically solved for Newtonian and power-law fluids assuming the absence of wall slip. Then, the theoretical predictions for the dependence of the squeeze force on the gap between plates were verified. Honey and the Newtonian plateaus of a shear-thinning ophthalmic ointment and a shear-thickening fumed silica suspension were employed as the Newtonian fluids. A foot cream and an ophthalmic ointment were utilized as the shear-thinning fluids. Finally, a fumed silica suspension was employed as the shear-thickening fluid. This study aimed to present and test an analytical solution for the SSRF problem that can be used for analyzing and predicting the behavior of the three most representative fluid viscous behaviors (i.e., Newtonian, shear-thinning, and shear-thickening) in 3D-flow situations.

II. EXPERIMENTAL

Rheological experiments were conducted on a controlled stress rheometer MARS III (Haake Thermo Electron Corporation GmbH, Karlsruhe, Germany). The sample was maintained at 20 °C using a Peltier system.

Steady flow curves were obtained using a cone-plate system with a 1° cone angle, 20 mm diameter, and 52 μm gap. The correlation between the apparent viscosity and

[a)]Dedicated to Nicolás M. Páez-Flor, Ph.D. In memoriam (1983–2023).
[b)]Author to whom correspondence should be addressed; electronic mail: fjrubio@uma.es

shear rate was recorded. The steady flow condition was assumed when the relative variation of the response, that is, shear stress, to each step by step applied shear rate was less than 1% for 10 s. This condition was easily achieved for the considered shear rate intervals. The liquid media used in this study were Newtonian eucalyptus honey (Apisol S.A., Valencia, Spain), two non-Newtonian shear-thinning fluids, that is, a moisturizing foot cream (Babaria, Berioska S.L., Valencia, Spain) and an ophthalmic ointment (Recugel®, Bausch + Lomb Inc., New Jersey, USA), and a shear-thickening suspension. The shear-thickening suspension was prepared by adding polypropylene glycol (PPG400, from Sigma-Aldrich, Spain) with an average molar mass of 400 g/mol to hydrophilic fumed silica particles (Aerosil®200, from Evonik, Germany) and then mixing at 800 rpm for 10 min with an RZR1 stirrer (Heidolph Instruments, Germany) using a PR30 pitched-blade impeller. The amount of the solid phase (A200® particles) in the liquid phase (PPG400) was 20%*w*/*w*, and a constant temperature of 20 °C was maintained during the experiment; thus, the shear-thickening suspension was labelled as 20A200PPG40020. The absence of wall slip in the rotational shear tests was verified by comparing the cone-plate results with the results of a plate-plate system with 20 mm (Fig. 1) and two different gaps (1 and 0.5 mm) [14]. Although the results do not prove the absence of wall slip for the SSFR rheological tests, they indicate the realization of such a condition, at least as a first approximation. Moreover, the nondependence of the results on the cone angle was validated for the cone-plate system with a 2° cone angle, 35 mm diameter, and 105 μm gap (Fig. 1).

The Newtonian behavior of the employed honey was confirmed (Fig. 2), with a constant viscosity value of $\eta_N = (22.0 \pm 0.5)$Pa s at 20 °C. Furthermore, the dependence of the foot cream viscosity (Fig. 2) on the shear rate was obtained under isothermal conditions (20 °C), and the results fitted very well to the power law ($R^2 = 0.9985$) in the full shear rate interval considered herein

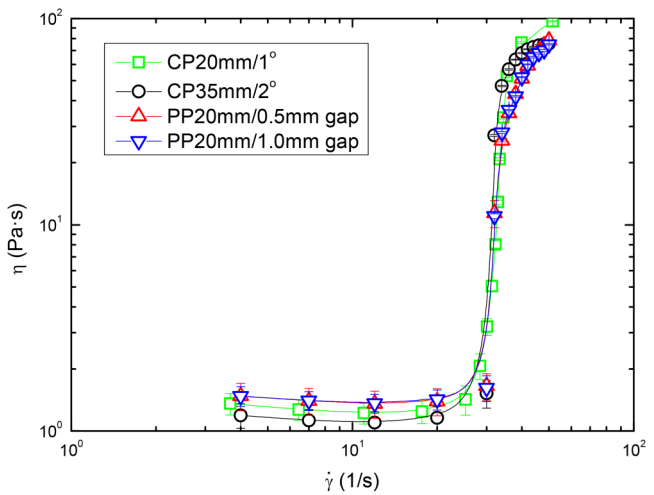

FIG. 1. Steady viscosity curves of 20A200PPG40020 suspension obtained using different geometries and gaps. The coincidence of the results indicates the nonslip condition at the walls and nondependence on the cone angle. Lines are included for guidance.

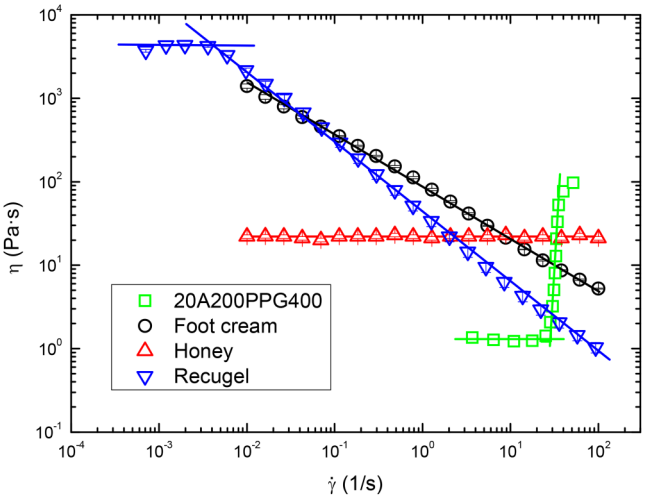

FIG. 2. Steady viscosity curves of the honey (Newtonian fluid), foot cream (shear-thinning fluid), Recugel® (Newtonian and shear-thinning fluids), and 20A200PPG400 suspension (Newtonian and shear-thickening fluids), $T = 20$ °C. Power law very well fitted the non-Newtonian behaviors in all cases.

($\eta(\dot\gamma) = (87.5 \pm 1.4)\dot\gamma^{-(0.62\pm0.01)}$). The ophthalmic ointment exhibited Newtonian behavior with a constant viscosity of $\eta_N = (4400 \pm 100)$Pa s at shear rates lower than 0.006 s^{-1} and well fitted the power law ($R^2 = 0.9993$) in the interval ($0.006 - 100\,s^{-1}$)($\eta(\dot\gamma) = (43.1 \pm 0.7)\dot\gamma^{-(0.86\pm0.01)}$). Moreover, the shear-thinning behavior of the ophthalmic ointment was more abrupt ($n = 0.14$) than that of the foot cream ($n = 0.38$). In principle, the consistencies of the two materials cannot be compared because their units are very different (Pa $s^{0.14}$ for the ophthalmic ointment and Pa $s^{0.38}$ for the foot cream). Nevertheless, as the numerical value of the consistency index coincided with the viscosity value when the shear rate was 1 s^{-1}, the foot cream was inferred to be more consistent than the ophthalmic ointment. Finally, the 20A200PPG40020 suspension displayed Newtonian behavior with a constant viscosity of $\eta_N = (1.31 \pm 0.05)$Pa s at shear rates lower than 20 s^{-1} and exhibited discontinuous shear-thickening behavior (Fig. 2) in a very narrow shear rate interval ($20 - 40\,s^{-1}$). Additionally, the results in this shear rate interval were fitted to a power law ($R^2 = 0.9532$), depicting the dependence $\eta(\dot\gamma) = (10^{-23} \pm 10^{-25})\dot\gamma^{(16\pm1)}$ of the viscosity with the shear rate.

The fluids were squeezed out using the axial test included in the rheometer's Rheowin 4.60 software. A previous study [15] found that better reproducible results were obtained with the rheometer MARS III when the squeeze velocity was controlled than when the squeeze force was monitored. Therefore, this study controlled the squeeze velocity using the constant area method between two parallel coaxial plates (Fig. 3), that is, while the lower plate was maintained stationary, the upper plate was displaced toward the lower plate under constant velocity. Prior to the SSRF test, a rotational shear stress was applied, which was maintained during the SSRF test until a steady state was achieved. This was done to develop the microstructure before the start of the SSRF test and maintain it during the SSRF test. The plate diameter was $2R_0 = 20$ mm and the initial gap was $h_0 = 1.5$ mm. Consequently, the geometric parameter $\zeta = \frac{h}{R_0}$ related to the

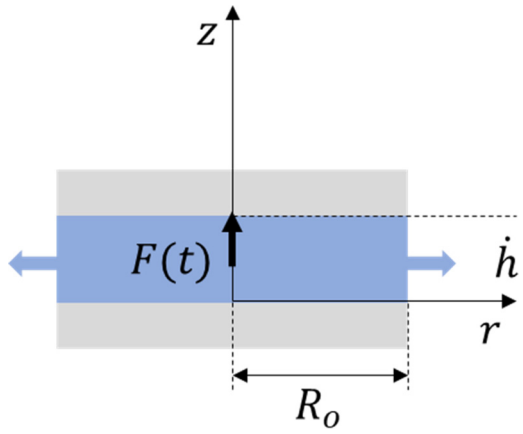

FIG. 3. Scheme of the squeeze flow between two axisymmetric circular flat plates. The sample radius (R_0) maintains constant being the gap between plates [$h(t)$], the independent variable, and the normal force [$F(t)$] exerted on the upper surface by the sample, the independent variable. For the selected coordinate system, the squeeze velocity $\dot{h}$ is negative.

variable gap during the squeeze and the plate radius was always sufficiently small; therefore, the terms of $\mathcal{O}(\zeta^2)$ in the movement equation could be neglected.

III. RESULTS AND DISCUSSION

A. Newtonian fluids

For Newtonian fluids, $\eta(II_{\dot{\gamma}}) = \eta_c = \eta_N$ and the movement Eqs. (A22) and (A23) (see Appendix) are

$$0 = -\frac{\mathrm{d}\hat{p}}{\mathrm{d}\hat{r}} + \frac{\partial^2 \hat{v}_r}{\partial \hat{z}^2}\ , \tag{1}$$

$$0 = \frac{\partial^2 \hat{v}_\theta}{\partial \hat{z}^2}. \tag{2}$$

Integrating Eq. (1) with respect to $\hat{z}$ and considering that $\hat{p} = \hat{p}(\hat{r})$,

$$\frac{\partial \hat{v}_r}{\partial \hat{z}} = \frac{\mathrm{d}\hat{p}}{\mathrm{d}\hat{r}}\hat{z} + C(\hat{r}, \hat{\theta}), \tag{3}$$

where $C(\hat{r}, \hat{\theta})$ is an integration constant. To determine the value of the constant, the symmetry condition $\frac{\partial \hat{v}_r}{\partial \hat{z}}\big|_{\hat{z}=\frac{1}{2}} = 0$ was used. Therefore,

$$\frac{\partial \hat{v}_r}{\partial \hat{z}} = \frac{\mathrm{d}\hat{p}}{\mathrm{d}\hat{r}}\left(\hat{z} - \frac{1}{2}\right). \tag{4}$$

Substitution of Eq. (4) in Eq. (A29) yielded

$$\frac{\mathrm{d}\hat{p}}{\mathrm{d}\hat{r}} = 6\hat{r}. \tag{5}$$

Once steady state was achieved, rotational shear stress $\tau_{\theta z}$ was generated and maintained. The microstructure developed in the material opposes the rotor plate with a normal stress $\tau_{zz} = -p + 2\eta_N \frac{\partial v_z}{\partial z}$. The second term was assumed to be negligible compared to the first term [16]; thus, the total normal force exerted by the liquid on the upper plate was dominated by the gauge hydrostatic pressure. Therefore,

$$F_z = \int_0^{R_o} p|_{z=h} 2\pi r \mathrm{d}r. \tag{6}$$

Integrating Eq. (6) by parts and using the boundary condition $p|_{z=h,\, r=R_o} = 0$, the following was obtained:

$$F_z = -\pi \int_0^{R_o} r^2 \frac{\mathrm{d}p}{\mathrm{d}r}\mathrm{d}r. \tag{7}$$

In terms of nondimensional variables with $\eta_c = \eta_N$, Eq. (7) transformed to

$$F_z = -\frac{\pi \eta_N \dot{h}}{h^3} R_o^4 \int_0^1 \hat{r}^2 \frac{\mathrm{d}\hat{p}}{\mathrm{d}\hat{r}}\mathrm{d}\hat{r}. \tag{8}$$

Substitution of Eq. (5) in Eq. (8) yielded the well-known Stefan equation [1],

$$F_z = -\frac{3}{2}\frac{\pi \eta_N \dot{h}}{h^3} R_o^4. \tag{9}$$

The results are justified as follows. The increase in the shear rate with decreasing gap did not influence the viscosity value simply because the fluid is Newtonian. Therefore, the superimposed rotational shear does not have any additional influence on the relationship between the squeeze force and velocity compared to squeeze test results in the absence of the superimposed rotational flow (Stefan equation). Figure 4 illustrates that the superimposed rotational shear does not modify the quantitative dependence of F_z with h, even when different shear stress values are applied. Linear plots [Fig. 4(a)] and log-log plots [Fig. 4(b)] are also presented to highlight the good fit of the model predictions [Eq. (9)] with the experimental results. Specifically, the slope of the $\log F - \log h$ plot $\left(\frac{d\log F_z}{d\log h} = -3\right)$ well agreed with the predictions of Eq. (9).

B. Power-law fluid

For power-law fluids, $\eta(\dot{\gamma}) = K\dot{\gamma}^{n-1}$, where K is the consistency and n is the power-law index. Substitution of Eqs. (A22) and (A23) into the motion equation yielded

$$\frac{\mathrm{d}\hat{p}}{\mathrm{d}\hat{r}} = \frac{K}{\eta_c}\frac{\partial}{\partial \hat{z}}\left(\dot{\gamma}^{n-1}\frac{\partial \hat{v}_r}{\partial \hat{z}}\right), \tag{10}$$

$$0 = \frac{\partial}{\partial \hat{z}}\left(\dot{\gamma}^{n-1}\frac{\partial \hat{v}_\theta}{\partial \hat{z}}\right). \tag{11}$$

Within the lubrication approximation, the following can be assumed [17]:

$$\dot{\gamma} = \sqrt{\dot{\gamma}_{rz}^2 + \dot{\gamma}_{\theta z}^2}. \tag{12}$$

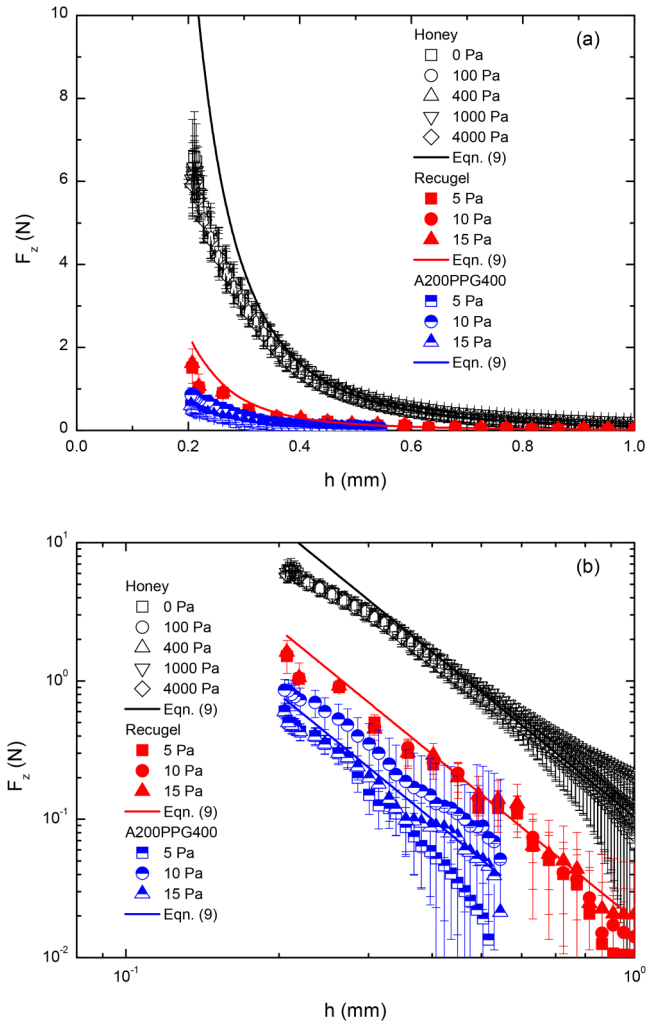

FIG. 4. Validation of Eq. (9) for the Newtonian behavior, $\dot{h} = -100\,\mu$m/s, $T = 20\,^{\circ}$C. (a) Linear and (b) log-log plots.

Substitution of $v_\theta = r\Omega_h(z)$ in Eq. (11) afforded

$$0 = \frac{\partial}{\partial z}\left(\dot{\gamma}^{n-1}\frac{\partial \Omega_h}{\partial z}\right). \tag{13}$$

Assuming the simple shear condition, $\frac{\partial \Omega_h}{\partial z} = \frac{\Omega_h}{h} \neq f(z)$. Equation (11) states that $\dot{\gamma}$ is not a function of z. Therefore, Eq. (10) was transformed to the simplest form,

$$\frac{\mathrm{d}\hat{p}}{\mathrm{d}\hat{r}} = \frac{K}{\eta_c}\dot{\gamma}^{n-1}\frac{\partial^2 \hat{v}_r}{\partial \hat{z}^2}. \tag{14}$$

Integrating Eq. (14) with respect to $\hat{z}$ provided

$$\frac{\partial \hat{v}_r}{\partial \hat{z}} = \frac{\eta_c}{K\dot{\gamma}^{n-1}}\frac{\mathrm{d}\hat{p}}{\mathrm{d}\hat{r}}\hat{z} + C(\hat{r}, \hat{\theta}), \tag{15}$$

where $C(\hat{r}, \hat{\theta})$ is the integration constant. To determine this constant, the symmetry condition $\frac{\partial \hat{v}_r}{\partial \hat{z}}\big|_{\hat{z}=\frac{1}{2}} = 0$ was employed. Therefore,

$$\frac{\partial \hat{v}_r}{\partial \hat{z}} = \frac{\eta_c}{K\dot{\gamma}^{n-1}}\frac{\mathrm{d}\hat{p}}{\mathrm{d}\hat{r}}\left(\hat{z} - \frac{1}{2}\right). \tag{16}$$

Substituting Eq. (16) in Eq. (A29), the following was obtained:

$$\frac{\mathrm{d}\hat{p}}{\mathrm{d}\hat{r}} = \frac{K\dot{\gamma}^{n-1}}{\eta_c}6\hat{r}. \tag{17}$$

Note that $\dot{\gamma}^{n-1}$ is a function of r to be determined. Since $\dot{\gamma}_{rz} = \frac{\partial v_r}{\partial z} = -\frac{r}{2}\frac{\mathrm{d}^2 v_z}{\mathrm{d}z^2}$ and $\dot{\gamma}_{\theta z} = \frac{\partial v_\theta}{\partial z} = r\frac{\Omega_h}{h}$, the generalized shear rate was

$$\dot{\gamma} = r\sqrt{\frac{1}{4}\left(\frac{\mathrm{d}^2 v_z}{\mathrm{d}z^2}\right)^2 + \left(\frac{\Omega_h}{h}\right)^2}. \tag{18}$$

Therefore,

$$\frac{\mathrm{d}\hat{p}}{\mathrm{d}\hat{r}} = 6\frac{K}{\eta_c}R_0^{n-1}\left[\frac{1}{4}\left(\frac{\mathrm{d}^2 v_z}{\mathrm{d}z^2}\right)^2 + \left(\frac{\Omega_h}{h}\right)^2\right]^{\frac{n-1}{2}}\hat{r}^n = A\hat{r}^n, \tag{19}$$

where $A = 6\frac{K}{\eta_c}R_0^{n-1}\left[\frac{1}{4}\left(\frac{\mathrm{d}^2 v_z}{\mathrm{d}z^2}\right)^2 + \left(\frac{\Omega_h}{h}\right)^2\right]^{\frac{n-1}{2}}$ does not depend on r. Equation (7) in terms of nondimensional variables is

$$F_z = -\frac{\pi\eta_c\dot{h}}{h^3}R_o^4\int_0^1 \hat{r}^2\frac{\mathrm{d}\hat{p}}{\mathrm{d}\hat{r}}\mathrm{d}\hat{r}. \tag{20}$$

The substitution of Eq. (19) in Eq. (20) afforded

$$F_z = -\frac{\pi\eta_c\dot{h}}{h^3}AR_o^4\int_0^1 \hat{r}^{n+2}\mathrm{d}\hat{r}. \tag{21}$$

Solving the integral in Eq. (21), the following was obtained:

$$F_z = -\frac{\pi\dot{h}}{h^3(n+3)}6KR_0^{n+3}\left[\frac{1}{4}\left(\frac{\mathrm{d}^2 v_z}{\mathrm{d}z^2}\right)^2 + \left(\frac{\Omega_h}{h}\right)^2\right]^{\frac{n-1}{2}}. \tag{22}$$

The derivative $\frac{\mathrm{d}^2 v_z}{\mathrm{d}z^2}$ needs to be determined to obtain a useful expression for the force exerted by the fluid opposite to the squeeze flow. Considering the Taylor expansion of v_z around $z = \frac{h}{2}$ and $h \ll R_0$, the dependence of $\frac{\mathrm{d}^2 v_z}{\mathrm{d}z^2}$ with z can be neglected. Therefore,

$$\frac{\mathrm{d}^2 v_z}{\mathrm{d}z^2} = C \Rightarrow \frac{\mathrm{d}v_z}{\mathrm{d}z} = Cz + D, \tag{23}$$

where C and D are constants. As $v_r(r, 0) = -\frac{r}{2}\frac{\mathrm{d}v_z}{\mathrm{d}z} = 0$, $D = 0$. Integration of Eq. (23) using the boundary conditions

Eq. (A19) yielded

$$v_z = \frac{\dot{h}}{h^2} z^2. \tag{24}$$

Therefore, the substitution of Eq. (24) in Eq. (22) afforded

$$F_z = -\frac{\pi \dot{h}}{h^3(n+3)} 6KR_0^{n+3} \left[\frac{1}{4}\left(\frac{\dot{h}}{h^2}\right)^2 + \left(\frac{\Omega_h}{h}\right)^2\right]^{\frac{n-1}{2}}. \tag{25}$$

Equation (25) reduces to the Newtonian prediction [Eq. (9)] when $n = 1$ and $K = \eta_N$, indicating that the superimposed rotation does not influence the squeeze flow behavior of Newtonian fluids.

The experimental results and theoretical predictions [Eq. (25)] for the dependence of the squeeze force on the gap for the SSRF of power-law fluids were compared. The predictions for both shear-thinning and shear-thickening behaviors were analyzed. Figure 5 displays the shear stress intervals where the shear-thinning and shear-thickening behaviors were observed. The shear-thinning behaviors of the foot cream and ophthalmic ointment were observed in the shear stress intervals (15 − 500 Pa) and (20 − 100 Pa), respectively, while the shear-thickening behavior of the 20A200PPG40020 suspension was observed in the shear stress interval (30 − 5000 Pa). Note that the superimposition of the shear stress instead of the shear rate to the squeeze flow was preferred as the employed rheometer in a stress-controlled device, which ensures that the squeezed microstructure was the same during all the SSRF tests.

The rotational term $\left(\frac{\Omega_h}{h}\right)$ in Eq. (25) was calculated from the experimental raw data (Table I). As shown in Fig. 6, this term slightly increased as the gap decreased for the shear-thinning fluids, and regardless of the superimposed rotational shear stress value, it was practically independent of the rotational shear stress and gap value for the shear-thickening fluid. These two significantly different variations can be justified as follows. When the rotational superimposed shear stress increased, the microstructure in the shear-thinning fluids weakened. Moreover, for a given gap value, the corresponding viscosity value decreased and the angular velocity increased. When the gap value decreased, the rotational term $\frac{\Omega_h}{h}$ increased. The observations for the shear-thickening fluid were very different. The 20A200PPG40020 suspension exhibited discontinuous shear-thickening behavior (Fig. 1). As shown in Fig. 7, for the interval of shear stress values where the 20A200PPG40020 suspension exhibited shear-thickening behavior in accordance with the power-law equation (30 − 2500)Pa, the shear rate variation range was extremely short (25 − 35 s^{-1}). Thus, despite the high variation in the superimposed shear stress values in the shear-thickening region, the variation in the corresponding rotational term was comparatively low.

The experimental results well qualitatively agreed the theoretical predictions obtained using Eq. (25) for the

TABLE I. Dependence of the rotational term on the gap.

σ (Pa)	$\frac{\Omega_h}{h}$ (rad/s · m)	r^2
Shear-thinning fluid (foot cream)		
50	$(26.7 \pm 0.6) + (315 \pm 8)\exp(-h/((2.66 \pm 0.06)\cdot 10^{-4}))$	0.9962
75	$(52.3 \pm 0.6) + (508 \pm 8)\exp(-h/((2.62 \pm 0.04)\cdot 10^{-4}))$	0.9985
100	$(138.3 \pm 0.7) + (830 \pm 8)\exp(-h/((2.74 \pm 0.03)\cdot 10^{-4}))$	0.9994
250	$(1322 \pm 9) + (6700 \pm 1400)\exp(-h/((1.3 \pm 0.1)\cdot 10^{-4}))$	0.9124
500	$(7290 \pm 40) + (12100 \pm 700)\exp(-h/((2.4 \pm 0.1)\cdot 10^{-4}))$	0.9836
Shear-thinning fluid (ophthalmic ointment)		
40	$(68 \pm 2) + (1280 \pm 40)\exp(-h/((2.0 \pm 0.1)\cdot 10^{-4}))$	0.9971
50	$(97 \pm 2) + (1790 \pm 50)\exp(-h/((1.8 \pm 0.1)\cdot 10^{-4}))$	0.9983
60	$(124 \pm 3) + (2180 \pm 70)\exp(-h/((1.9 \pm 0.1)\cdot 10^{-4}))$	0.9982
Shear-thickening fluid (20A200PPG40020)		
100	3600 ± 300	—
500	3800 ± 200	—
1000	3900 ± 400	—
2500	4100 ± 600	—

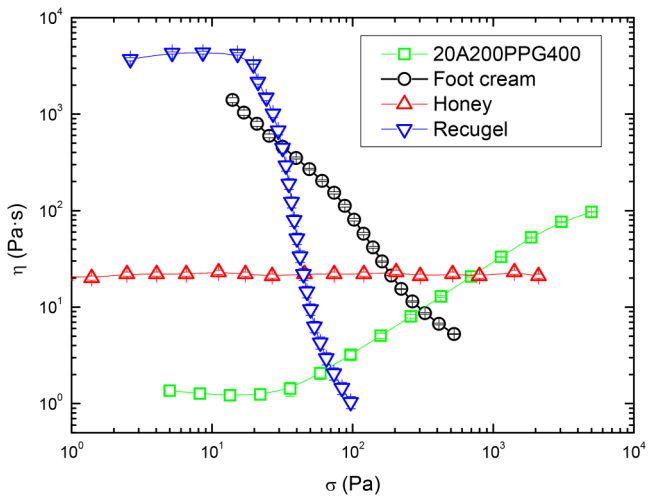

FIG. 5. Steady apparent viscosity vs shear stress curves displaying Newtonian and non-Newtonian behaviors, $T = 20\,^{\circ}\mathrm{C}$. Lines are included for guidance.

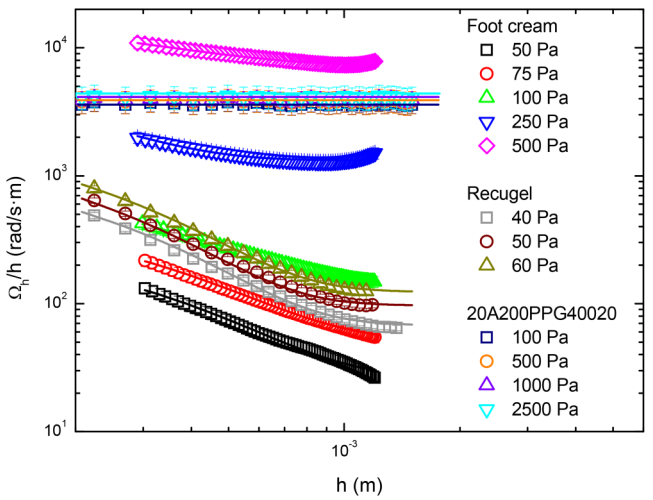

FIG. 6. Rotational term $\left(\frac{\Omega_h}{h}\right)$ vs the plate gap. This term decreases with the gap for shear-thinning fluids but stays practically constant with decreasing gap for the shear-thickening fluid (see the text for a possible justification of this behavior), $T = 20\,^{\circ}\mathrm{C}$. The lines correspond to exponential decay fits.

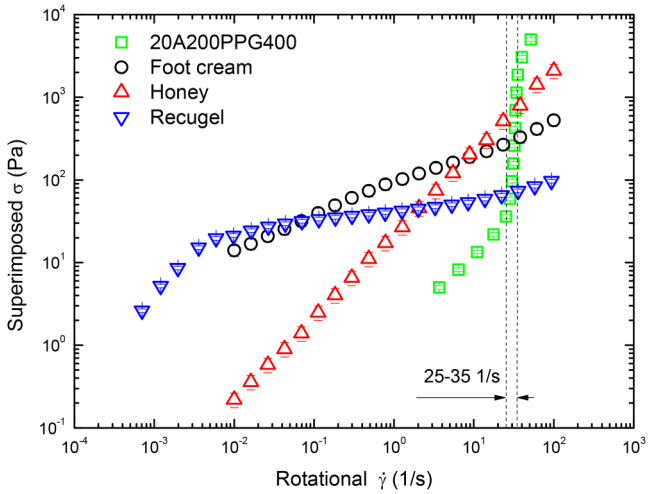

FIG. 7. Steady flow curves of the 20A200PPG400 suspension, foot cream, Recugel®, and honey ($T = 20\,^{\circ}\mathrm{C}$).

shear-thinning (Figs. 8 and 9) and shear-thickening (Fig. 10) fluids. For the shear-thinning fluids, the viscosity decreased with increasing superimposed rotational shear stress, resulting in a less pronounced increases in the normal force with

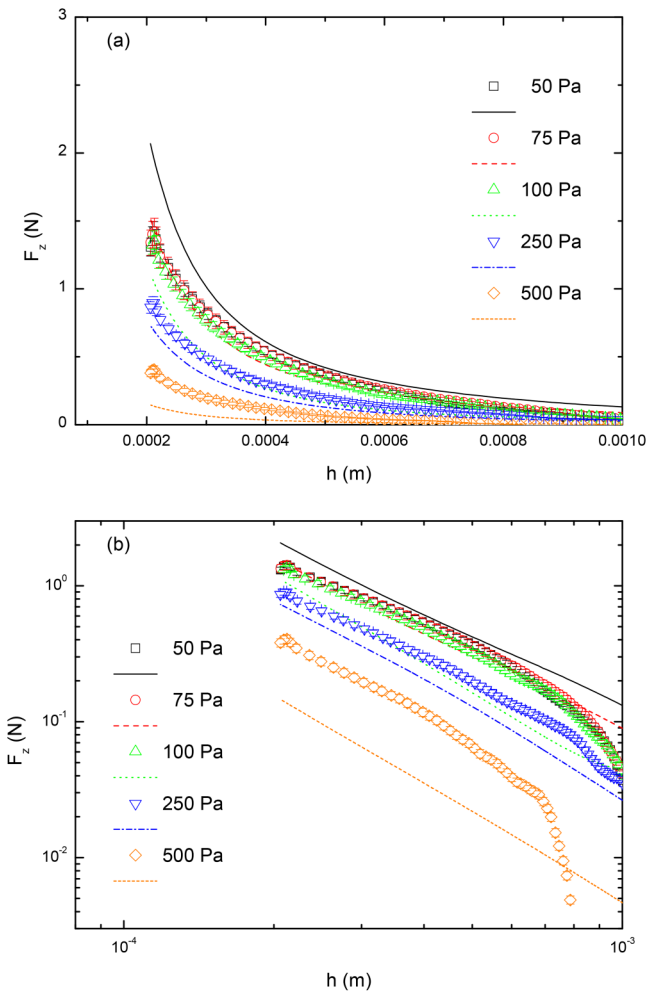

FIG. 8. Experimental results and theoretical predictions [Eq. (25)] of the dependence of the normal force on the gap value for superimposed rotational and squeeze flow of the shear-thinning foot cream. $\dot{h} = -100\,\mu$m/s; $T = 20\,^{\circ}\mathrm{C}$. (a) Linear and (b) log-log plots.

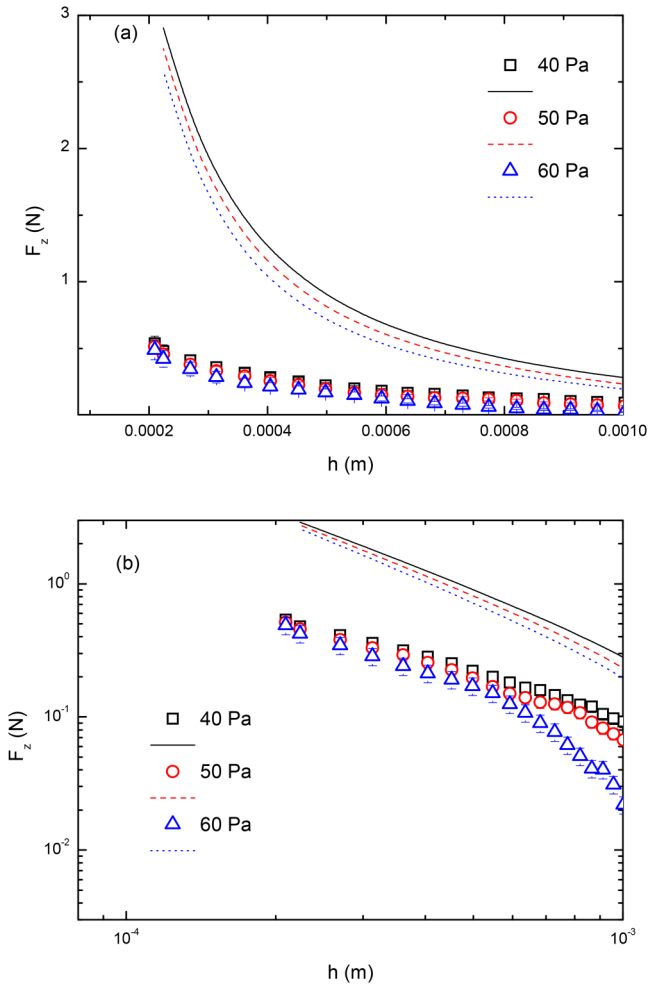

FIG. 9. Experimental results and theoretical predictions [Eq. (25)] of the dependence of the normal force on the gap value for superimposed rotational and squeeze flow of the shear-thinning Recugel®. $\dot{h} = -100\,\mu$m/s; $T = 20\,^{\circ}\mathrm{C}$. (a) Linear and (b) log-log plots.

decreasing gap value. In contrast, for the shear-thickening fluid, the viscosity increased with the superimposed rotational shear stress, resulting in the increase in the normal force based on the squeeze flow corresponding to the gap value. This denotes that the energy dissipation in hydraulic dumpers using shear-thickening fluids will be more effective when the superimposed rotational shear stress is higher. Certainly, the superposition of the rotational shear stress will incur some costs, which could make a device based on this idea unviable. In other words, expending energy (superimposed rotation) to dissipate energy (squeeze flow) sounds absurd. Therefore, superimposed rotation without an additional energetic spending needs to be realized, but this is matter for inventors.

However, the quantitative agreement between experimental results and theoretical prediction [Eq. (25)] was not so good for Recugel® probably due to typical wall slip observed in gels [18] but not considered in the theoretical development here presented. The existence of wall slip in Recugel® results was determined following Yoshimura and Prud'homme analysis [19] comparing the results of steady flow curves obtained using plate-plate geometry of 20 mm diameter and two different gaps (1 and 0.5 mm). According

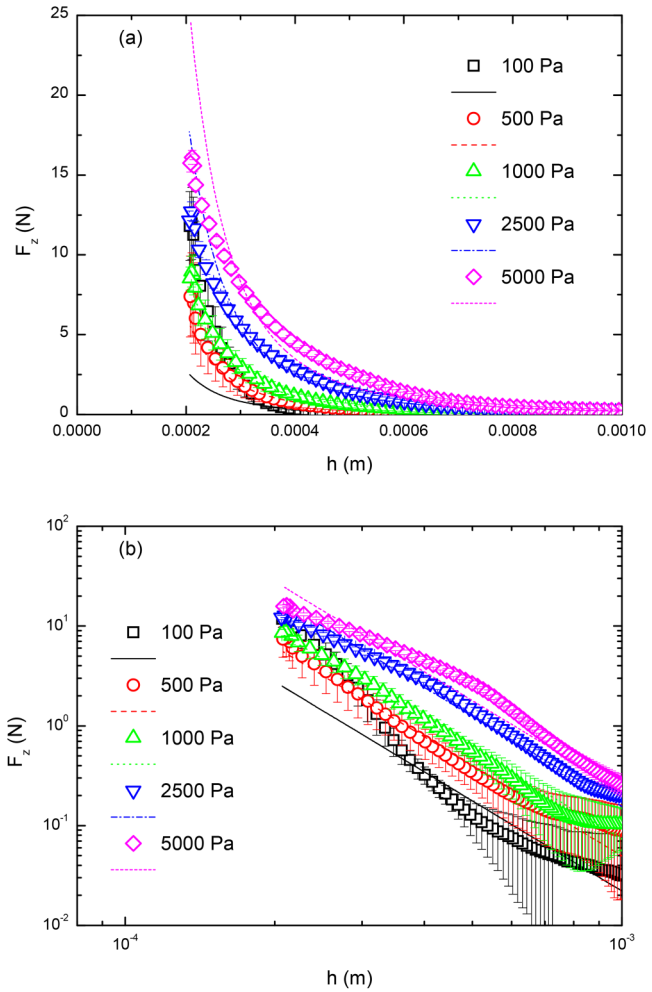

FIG. 10. Experimental results and theoretical predictions [Eq. (25)] of the dependence of the normal force on the gap value for superimposed rotational and squeeze flow of the shear-thickening 20A200PPG400 suspension. $\dot{h} = -100\,\mu$m/s; $T = 20\,^{\circ}$C. (a) Linear and (b) log-log plots.

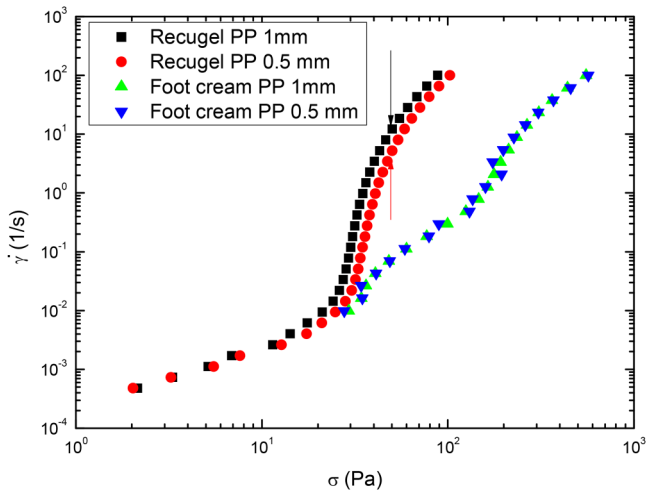

FIG. 11. Steady flow curves of Recugel® and the foot cream obtained using plate-plate geometry with two different gaps. The coincidence of the results indicates that no slip at the wall condition is accomplished. Note the difference in the shear rate values corresponding to the same applied shear stress value with different plate-plate gaps. Error bars, lower than 5%, were omitted for clarity.

to these authors, the actual shear rate ($\dot{\gamma}_R$) at the rim of a plate-plate of radius R is related to two apparent shear rate values corresponding to different gaps between plates,

$$\dot{\gamma}_R(\sigma_R) = \frac{H_1\dot{\gamma}_{R1}(\sigma_R) - H_2\dot{\gamma}_{R2}(\sigma_R)}{H_1 - H_2}, \tag{26}$$

where $\dot{\gamma}_{R1}$ and $\dot{\gamma}_{R2}$ are the apparent shear rates at the rim of plates separated distances H_1 and H_2, respectively. The coincidence of $\dot{\gamma}_{R1}$ and $\dot{\gamma}_{R2}$ for a given shear stress value σ_R will imply the absence of wall slip for the plate-plate geometry. As can be seen in Fig. 11, steady flow curves obtained with two PP configurations (1 and 0.5 mm gap) clearly coincide in the case of the foot cream, but some discrepancies are evident in the case of Recugel®. These results suggest the existence of wall slip in the last case, justifying the lack of quantitative agreement observed in Fig. 9.

IV. CONCLUSIONS

The theoretical predictions for SSRF were verified using a plate-plate system with Newtonian and power-law fluids. The response of the Newtonian fluids was independent of the superimposed rotational shear stress values. In contrast, for the power-law fluids, the superimposed stress influenced the variation in the squeeze force with the gap value. These very different behaviors stem from the viscosity dependence with shear characterizing each time-independent viscous behavior (Newtonian, shear-thinning, and shear-thickening).

ACKNOWLEDGMENTS

The authors gratefully acknowledge the Consejería de Economía, Innovación, Ciencia y Empleo (Junta de Andalucía, Spain) for providing funding under Grant No. PROYEXCEL_00181 for support of this project. The authors thank the Universidad de Málaga for providing funding for the Open Access charge. The authors wish to acknowledge valuable comments by one of the reviewers.

AUTHOR DECLARATIONS

Conflict of Interest

The authors have no conflicts to disclose.

DATA AVAILABILITY

The data that support the findings of this study are available from the corresponding author upon reasonable request.

APPENDIX: NONDIMENSIONAL GOVERNING EQUATIONS

When the upper plate simultaneously rotates and moves downward, the response against the squeezing deformation of the microstructure generated by the shear stress can be studied. According to the cylindrical polar coordinate system

(r, θ, z), the SSRF velocity vector is (Fig. 3)

$$\vec{v}(r, z) = \begin{pmatrix} v_r \\ v_\theta \\ v_z \end{pmatrix}. \tag{A1}$$

Therefore, the conservation of mass of an incompressible fluid in terms of the continuity equation is as follows:

$$\nabla \cdot \vec{v} = \frac{1}{r}\frac{\partial (r v_r)}{\partial r} + \frac{1}{r}\frac{\partial v_\theta}{\partial \theta} + \frac{\partial v_z}{\partial z} = 0. \tag{A2}$$

Moreover, neglecting the gravitational forces and inertia, the conservation of momentum equation is

$$0 = \nabla \cdot \boldsymbol{\tau}, \tag{A3}$$

where $\boldsymbol{\tau} = -p\boldsymbol{I} + \boldsymbol{\sigma}$ is the stress tensor, with p representing the hydrostatic pressure and $\boldsymbol{\sigma}$ representing the deviatoric or viscous stress tensor. The three components of Eq. (A3) are relevant for SSRF [20],

$$0 = -\frac{\partial p}{\partial r} + \frac{1}{r}\frac{\partial (r\sigma_{rr})}{\partial r} + \frac{1}{r}\frac{\partial \sigma_{r\theta}}{\partial \theta} + \frac{\partial \sigma_{rz}}{\partial z} - \frac{\sigma_{\theta\theta}}{r}, \tag{A4}$$

$$0 = -\frac{1}{r}\frac{\partial p}{\partial \theta} + \frac{1}{r^2}\frac{\partial (r^2\sigma_{r\theta})}{\partial r} + \frac{1}{r}\frac{\partial \sigma_{\theta\theta}}{\partial \theta} + \frac{\partial \sigma_{\theta z}}{\partial z}, \tag{A5}$$

$$0 = -\frac{\partial p}{\partial z} + \frac{1}{r}\frac{\partial (r\sigma_{rz})}{\partial r} + \frac{1}{r}\frac{\partial \sigma_{\theta z}}{\partial \theta} + \frac{\partial \sigma_{zz}}{\partial z}. \tag{A6}$$

Equations (A2) and (A4)–(A6) can be adequately scaled to obtain useful nondimensional equations. Based on Muravleva's analysis [21], the lengths are scaled with the disk radius R_0 in the r direction $\left(\hat{r} = \frac{r}{R_0}\right)$ and with the distance between disks h in the z direction $\left(\hat{z} = \frac{z}{h}\right)$. Additionally, the angle is scaled with $\frac{\dot{\gamma}_{R_o}}{h}h$, where $\dot{\gamma}_{R_o} = R_o\frac{\Omega_h}{h}$ is the rotational shear rate at the disk rim and Ω_h is the angular velocity of the rotor when the gap is h, that is, $\left(\hat{\theta} = \frac{\theta \dot{h}}{\dot{\gamma}_{R_o} h}\right)$. Velocities are scaled with the squeeze velocity $\dot{h}$ in the z direction $\left(\hat{v}_z = \frac{v_z}{\dot{h}}\right)$, with the compression rate $\left(\dot{\varepsilon} = \frac{\dot{h}}{h}\right)$ times the disk radius $R_0(\dot{h}R_0/h)$ in the r direction $\left(\hat{v}_r = v_r\frac{h}{R_0\dot{h}}\right)$, and with the shear rate at the rim times the disk radius $(\dot{\gamma}_{R_o}R_0)$ in the θ direction $\left(\hat{v}_\theta = \frac{v_\theta}{R_0\dot{\gamma}_{R_o}}\right)$. The pressure is scaled with $\eta_c\dot{h}R_0^2/h^3$, that is, $\left(\hat{p} = \frac{ph^3}{\eta_c\dot{h}R_0^2}\right)$, where η_c is some fluid characteristic viscosity value. Finally, the shear stress σ_{rz} is scaled with $\eta_c\dot{h}R_0/h^2$, but shear stresses $\sigma_{r\theta}$ and $\sigma_{z\theta}$ are scaled with $\eta_c\dot{\gamma}_{R_o}R_0/h$ and normal stresses are scaled with $\eta_c\dot{h}/h$. Consequently, the nondimensional continuity and movement equations are

$$\frac{1}{\hat{r}}\frac{\partial (\hat{r}\hat{v}_r)}{\partial \hat{r}} + \frac{1}{\hat{r}}\frac{\partial \hat{v}_\theta}{\partial \hat{\theta}} + \frac{\partial \hat{v}_z}{\partial \hat{z}} = 0, \tag{A7}$$

$$0 = -\frac{\partial \hat{p}}{\partial \hat{r}} + \zeta^2\frac{1}{\hat{r}}\frac{\partial (\hat{r}\hat{\sigma}_{rr})}{\partial \hat{r}} + \zeta\frac{1}{\hat{r}}\frac{\partial \hat{\sigma}_{r\theta}}{\partial \hat{\theta}} + \frac{\partial \hat{\sigma}_{rz}}{\partial \hat{z}} - \zeta^2\frac{\hat{\sigma}_{\theta\theta}}{\hat{r}}, \tag{A8}$$

$$0 = -\frac{1}{\hat{r}}\frac{\partial \hat{p}}{\partial \hat{\theta}} + \zeta\xi^2\frac{1}{\hat{r}^2}\frac{\partial (\hat{r}^2\hat{\sigma}_{r\theta})}{\partial \hat{r}} + \zeta^2\frac{1}{\hat{r}}\frac{\partial \hat{\sigma}_{\theta\theta}}{\partial \hat{\theta}} + \xi^2\frac{\partial \hat{\sigma}_{\theta z}}{\partial \hat{z}}, \tag{A9}$$

$$0 = -\frac{\partial \hat{p}}{\partial \hat{z}} + \zeta^2\frac{1}{\hat{r}}\frac{\partial (\hat{r}\hat{\sigma}_{rz})}{\partial \hat{r}} + \zeta^2\frac{1}{\hat{r}}\frac{\partial \hat{\sigma}_{\theta z}}{\partial \hat{\theta}} + \zeta^2\frac{\partial \hat{\sigma}_{zz}}{\partial \hat{z}}. \tag{A10}$$

As previously indicated, $\zeta = \frac{h}{R_0}$ is a geometric factor that associates the gap with the disk radius. Moreover, $\xi = \frac{\dot{\gamma}_{R_o}}{\dot{\varepsilon}}$ is a velocity factor that associates the rotational shear rate at the disk rim with the compression rate $\dot{\varepsilon}$. As ζ is always lower than 0.15, the $\mathcal{O}(\zeta^2)$ terms in Eqs. (A8)–(A10) can be neglected, resulting in the following simplified expressions:

$$0 = -\frac{\partial \hat{p}}{\partial \hat{r}} + \zeta\frac{1}{\hat{r}}\frac{\partial \hat{\sigma}_{r\theta}}{\partial \hat{\theta}} + \frac{\partial \hat{\sigma}_{rz}}{\partial \hat{z}}, \tag{A11}$$

$$0 = -\frac{1}{\hat{r}}\frac{\partial \hat{p}}{\partial \hat{\theta}} + \zeta\xi^2\frac{1}{\hat{r}^2}\frac{\partial (\hat{r}^2\hat{\sigma}_{r\theta})}{\partial \hat{r}} + \xi^2\frac{\partial \hat{\sigma}_{\theta z}}{\partial \hat{z}}, \tag{A12}$$

$$0 = -\frac{\partial \hat{p}}{\partial \hat{z}}. \tag{A13}$$

Equation (A13) yields that $\hat{p} \neq \hat{p}(\hat{z})$. Furthermore, the condition $\frac{\partial \hat{p}}{\partial \theta} = 0$ is realized because the rotational superimposed flow is a drag flow. Therefore, $\hat{p} = \hat{p}(\hat{r})$, and Eq. (A12) reads

$$0 = \zeta\frac{1}{\hat{r}^2}\frac{\partial (\hat{r}^2\hat{\sigma}_{r\theta})}{\partial \hat{r}} + \frac{\partial \hat{\sigma}_{\theta z}}{\partial \hat{z}}. \tag{A14}$$

To continue with this analysis, the constitutive equation of the fluid needs to be determined. Considering the study scope, the fluid is assumed to be inelastic and assumed to obey the generalized Newtonian fluid constitutive equation,

$$\boldsymbol{\sigma} = \eta(II_{\dot{\gamma}})\dot{\boldsymbol{\gamma}}, \tag{A15}$$

where $II_{\dot{\gamma}}$ is the second invariant of the strain rate tensor. In the absence of slip, $v_r = v_r(r, z)$, $v_\theta = v_\theta(r, z)$, and

$v_z = v_z(z)$. Therefore, the strain rate tensor is [20]

$$\dot{\gamma} = \begin{pmatrix} 2\frac{\partial v_r}{\partial r} & \frac{\partial v_\theta}{\partial r} - \frac{v_\theta}{r} & \frac{\partial v_r}{\partial z} \\ \frac{\partial v_\theta}{\partial r} - \frac{v_\theta}{r} & 2\frac{v_r}{r} & \frac{\partial v_\theta}{\partial z} \\ \frac{\partial v_r}{\partial z} & \frac{\partial v_\theta}{\partial z} & 2\frac{\partial v_z}{\partial z} \end{pmatrix}. \tag{A16}$$

Additionally, some assumptions about the $v_r(r, z)$, $v_\theta(r, z)$, and $v_z(z)$ functions must be imposed to continue with this analysis. Specifically, the following is reasonable to assume:

$$v_\theta(r, z) = r\Omega_h(z). \tag{A17}$$

Note that the $\Omega_h(z)$ dependence denotes that the angular velocity at each z plane is different due to the friction between the fluid layers. Moreover, the maximum angular velocity is generally a function of h. In other words, the angular velocity of the rotor varies as the gap decreases due to the eventual variation in the fluid viscosity. Substitution of Eq. (A17) into the continuity Eq. (A2) yields the radial component of the velocity,

$$v_r(r,\ z) = -\frac{r}{2}\frac{dv_z}{dz}. \tag{A18}$$

The following boundary conditions are also included in the analysis:

$$\left.\begin{array}{c} v_r(z=0) = v_\theta(z=0) = v_z(z=0) = v_r(z=h) = \Omega_h(z=0) = 0 \\ v_z(z=h) = \dot{h} \end{array}\right\}. \tag{A19}$$

As $v_\theta(r, z) \propto r$, $\frac{\partial v_\theta}{\partial r} = \frac{v_\theta}{r}$. Furthermore, the complete absence of slip at the solid-liquid interfaces implies that the shear deformation appears in the r and θ directions, with z being the gradient direction in both cases, that is,

$$\dot{\gamma} = \begin{pmatrix} 2\frac{\partial v_r}{\partial r} & 0 & \frac{\partial v_r}{\partial z} \\ 0 & 2\frac{v_r}{r} & \frac{\partial v_\theta}{\partial z} \\ \frac{\partial v_r}{\partial z} & \frac{\partial v_\theta}{\partial z} & 2\frac{\partial v_z}{\partial z} \end{pmatrix}. \tag{A20}$$

Here, $\frac{\partial \hat{v}_r}{\partial \hat{z}} = \hat{\dot{\gamma}}_{rz} = \frac{h^2}{hR_o}\dot{\gamma}_{rz} = \frac{h^2}{hR_o}\frac{\partial v_r}{\partial z}$ is the nondimensional squeeze shear rate and $\frac{\partial \hat{v}_\theta}{\partial \hat{z}} = \hat{\dot{\gamma}}_{\theta z} = \frac{h^2}{\Omega R_o^2}\dot{\gamma}_{\theta z} = \frac{h^2}{\Omega R_o^2}\frac{\partial v_\theta}{\partial z}$ is the nondimensional rotational shear rate. Substitution of Eq. (A20) into Eq. (A15) yields the deviatoric stress tensor components,

$$\left.\begin{array}{c} \sigma_{rr} = \eta(II_{\dot{\gamma}})2\frac{\partial v_r}{\partial r} \\ \sigma_{\theta\theta} = \eta(II_{\dot{\gamma}})2\frac{v_r}{r} \\ \sigma_{zz} = \eta(II_{\dot{\gamma}})2\frac{\partial v_z}{\partial z} \\ \sigma_{rz} = \eta(II_{\dot{\gamma}})\frac{\partial v_r}{\partial z} \\ \sigma_{\theta z} = \eta(II_{\dot{\gamma}})\frac{\partial v_\theta}{\partial z} \\ \sigma_{r\theta} = 0 \end{array}\right. . \tag{A21}$$

The nondimensional stress components are substituted into Eqs. (A11) and (A14), yielding

$$0 = -\frac{d\hat{p}}{d\hat{r}} + \frac{\partial}{\partial \hat{z}}\left(\frac{\eta(II_{\dot{\gamma}})}{\eta_c}\frac{\partial \hat{v}_r}{\partial \hat{z}}\right), \tag{A22}$$

$$0 = \frac{\partial}{\partial \hat{z}}\left(\frac{\eta(II_{\dot{\gamma}})}{\eta_c}\frac{\partial \hat{v}_\theta}{\partial \hat{z}}\right). \tag{A23}$$

The nondimensional continuity equation is

$$\frac{1}{\hat{r}}\frac{\partial(\hat{r}\hat{v}_r)}{\partial \hat{r}} + \frac{d\hat{v}_z}{d\hat{z}} = 0. \tag{A24}$$

Equation (A24) is integrated with respect to $\hat{z}$ from 0 ($z = 0$) to 1 ($z = h$) [22] using the boundary conditions, $\hat{v}_z(\hat{z} = 0) = 0$ and $\hat{v}_z(\hat{z} = 1) = 1$,

$$\int_0^1 \frac{1}{\hat{r}}\frac{\partial(\hat{r}\hat{v}_r)}{\partial \hat{r}}\partial\hat{z} + \int_0^1 \frac{d\hat{v}_z}{d\hat{z}}d\hat{z} = 0. \tag{A25}$$

Therefore,

$$\frac{\partial}{\partial \hat{r}}\left(\hat{r}\int_0^1 \hat{v}_r\partial\hat{z}\right) = -\hat{r}. \tag{A26}$$

Integration of Eq. (A26) with respect to $\hat{r}$ from the symmetry axis ($\hat{r} = 0$) yields

$$\int_0^1 \hat{v}_r\partial\hat{z} = -\frac{\hat{r}}{2}. \tag{A27}$$

The partial integration of Eq. (A27) affords

$$\hat{v}_r(\hat{z} = 1) - \int_0^1 \hat{z}\frac{\partial \hat{v}_r}{\partial \hat{z}}\partial\hat{z} = -\frac{\hat{r}}{2}. \tag{A28}$$

No-slip conditions are assumed at the solid-liquid interfaces [Eq. (A19)]. Subsequently, the boundary condition

$\hat{v}_r(\hat{z}=1)=0$ is used to obtain

$$\int_0^1 \hat{z}\frac{\partial \hat{v}_r}{\partial \hat{z}}\partial \hat{z}=\frac{\hat{r}}{2}. \tag{A29}$$

REFERENCES

[1] Stefan, J., "Versuche über die scheinbare Adhäsion," Ann. Phys. **230**, 316–318 (1875).

[2] Scott, J. R., "Theory and application of the parallel-plate plastimeter," Trans. Inst. Rubber Ind. **7**, 169–175 (1931).

[3] Sherwood, J. D., and D. Durban, "Squeeze flow of a power-law viscoplastic solid," J. Non-Newton. Fluid Mech. **62**(1), 35–54 (1996).

[4] Meeten, G., "Constant-force squeeze flow of soft solids," Rheol. Acta **41**(6), 557–566 (2002).

[5] Servais, C., A. Luciani, and J.-A. E. Månson, "Squeeze flow of concentrated long fibre suspensions: Experiments and model," J. Non-Newton. Fluid Mech. **104**(2–3), 165–184 (2002).

[6] Collomb, J., F. Chaari, and M. Chaouche, "Squeeze flow of concentrated suspensions of spheres in Newtonian and shear-thinning fluids," J. Rheol. **48**(2), 405–416 (2004).

[7] Li, Z., and X. Li, "Squeeze flow of viscoplastic cement-based extrudate," J. Eng. Mech. **133**(9), 1003–1008 (2007).

[8] Kraiem, A., A. Ayadi, and N. Elkissi, "Squeeze flow and rheological characterization of pure bitumen and bitumen mixed with kaolin," Korea-Aust. Rheol. J. **34**(3), 211–222 (2022).

[9] Gong, X., Q. Chen, M. Liu, S. Cao, S. Xuan, and W. Jiang, "Squeeze flow behavior of shear thickening fluid under constant volume," Smart Mater. Struct. **26**(6), 065017 (2017).

[10] Kim, J. H., and K. H. Ahn, "A new instrument for dynamic helical squeeze flow which superposes oscillatory shear and oscillatory squeeze flow," Rev. Sci. Instrum. **83**(8), 085105 (2012).

[11] Ovarlez, G., Q. Barral, and P. Coussot, "Three-dimensional jamming and flows of soft glassy materials," Nat. Mater. **9**(2), 115–119 (2010).

[12] Laun, H. M., M. Rady, and O. Hassager, "Analytical solutions for squeeze flow with partial wall slip," J. Non-Newton. Fluid Mech. **81**(1–2), 1–15 (1999).

[13] Yang, S.-P., and K.-Q. Zhu, "Note on a paper by Laun: The squeeze force for a power law fluid," J. Non-Newton. Fluid Mech. **132**(1–3), 84–85 (2005).

[14] Rubio-Hernández, F. J., J. H. Sánchez-Toro, and N. M. Páez-Flor, "Testing shear thinning/thixotropy and shear thickening/antithixotropy relationships in a fumed silica suspension," J. Rheol. **64**(4), 785–797 (2020).

[15] Rubio-Hernández, F. J., J. F. Velázquez-Navarro, M. Rodríguez-Lara, A. I. Gómez-Merino, M. Jebali, and J. J. Jiménez-Galea, "A comparison between results from squeeze flow tests of fumed silica shear thickening suspensions," in *Proceedings of the Iberian Meeting on Rheology (IBEREO 2024)*, Springer Proceedings in Materials (SPM) Series, Lisbon, Portugal, 4–6 September 2024 (Springer, Cham, Switzerland, 2024).

[16] Engmann, J., C. Servais, and A. S. Burbidge, "Squeeze flow theory and applications to rheometry: A review," J. Non-Newton. Fluid Mech. **132**(1–3), 1–27 (2005).

[17] Binding, D. M., J. M. Davies, and K. Walters, "Elastico-viscous squeeze films. Part 2. Superimposed rotation," J. Non-Newton. Fluid Mech. **1**(3), 259–275 (1976).

[18] Quan, L., and D. M. Kalyon, "Parallel-disk viscometry of a viscoplastic hydrogel: Yield stress and other parameters of shear viscosity and wall slip," Gels **8**(4), 230-1–230-33 (2022).

[19] Yoshimura, A., and R. K. Prud'homme, "Wall slip corrections for Couette and parallel disk viscometers," J. Rheol. **32**(1), 53–67 (1988).

[20] Bird, R. B., R. C. Armstrong, and O. Hassager, *Dynamics of Polymeric Liquids* (John Wiley & Sons, Hoboken, New Jersey, 1987), Vol. 1.

[21] Muravleva, L., "Axisymmetric squeeze flow of a viscoplastic Bingham medium," J. Non-Newton. Fluid Mech. **249**, 97–120 (2017).

[22] Brindley, G., J. M. Davies, and K. Walters, "Elastico-viscous squeeze films. Part I," J. Non-Newton. Fluid Mech. **1**(1), 19–37 (1976).